Probing Crystallinity and Grain Structure of 2D Materials and 2D-Like Van der Waals Heterostructures by Low-Voltage Electron Diffraction

Johannes Müller,* Max Heyl, Thorsten Schultz, Kristiane Elsner, Marcel Schloz, Steffen Rühl, Hélène Seiler, Norbert Koch, Emil J. W. List-Kratochvil, and Christoph T. Koch

4D scanning transmission electron microscopy (4D-STEM) is a powerful method for characterizing electron-transparent samples with down to sub-Ångstrom spatial resolution. 4D-STEM can reveal local crystallinity, orientation, grain size, strain, and many more sample properties by rastering a convergent electron beam over a sample area and acquiring a transmission diffraction pattern (DP) at each scan position. These patterns are rich in information about the atomic structure of the probed volume, making this technique a potent tool to characterize even inhomogeneous samples. 4D-STEM can also be used in scanning electron microscopes (SEMs) by placing an electron-sensitive camera below the sample. 4D-STEM-in-SEMs is ideally suited to characterize 2D materials and 2D-like van der Waals heterostructures (vdWH) due to their inherent thickness of a few nanometers. The lower accelerating voltage of SEMs leads to strong scattering even from monolayers. The large field of view and down to sub-nm spatial resolution of SEMs are ideal to map properties of the different constituents of 2D-like vdWH by probing their combined sample volume. A unique 4D-STEM-in-SEM system is applied to reveal the single crystallinity of MoS_2 exfoliated with gold-mediation as well as the crystal orientation and coverage of both components of a $C60/MoS_2$ vdWH are determined.

have attracted vigorous interest in recent years.[1–4] Transmission electron microscopy (TEM) is ideal to study the crystalline structure of 2D materials due to their sub-Ångstrom spatial resolution.[5] 2D-like vdWHs, meaning stacks of 2D materials or 2D materials decorated with thin films of organic molecules (also called 0D–2D vdWH) are also ideally suited to reveal their structure by low-voltage electron microscopy, since theirthickness is inherently limited to a few nanometers.[4,6] In many cases, the properties of 2D-like vdWH depend on the relative in-plane orientation that their constituents have with respect to each other,[7] a property that is not observable from techniques that are only sensitive to the surface. But also other microscopic structural properties like the local layer arrangement, grain boundaries, strain, and more have an effect on the macroscopic materials properties. Being able to probe these microscopic structural properties is thus essential for optimizing the functionality of corresponding devices and guiding their fabrication.

1. Introduction

Van der Waals heterostructures (vdWH) of 2D materials, the tunability of the fundamental interactions at their (hybrid) interfaces, and their potential for devices with unique functionalities

1.1. Introduction to 4D-STEM

4D scanning transmission electron microscopy (4D-STEM) is a powerful method for characterizing material properties, such as the crystal structure of samples that have a thickness of a few tens

J. Müller, M. Heyl, K. Elsner, M. Schloz, S. Rühl, N. Koch,
E. J. W. List-Kratochvil, C. T. Koch
Department of Physics & IRIS Adlershof
Humboldt-Universität zu Berlin
Newtonstraße 15, Berlin 12489, Germany
E-mail: johannes.mueller@physik.hu-berlin.de

The ORCID identification number(s) for the author(s) of this article can be found under https://doi.org/10.1002/pssa.202300148.

M. Heyl, S. Rühl, E. J. W. List-Kratochvil
Department of Chemistry
Humboldt-Universität zu Berlin
Zum Großen Windkanal 2, Berlin 12489, Germany

T. Schultz, N. Koch, E. J. W. List-Kratochvil
Helmholtz-Zentrum Berlin für Materialien und Energie GmbH
Hahn-Meitner-Platz 1, Berlin 14109, Germany

H. Seiler
Department of Physics
Free University of Berlin
Arnimallee 14, 14195 Berlin, Germany

H. Seiler
Fritz Haber Institute of the Max Planck Society
Faradayweg 4-6, 14195 Berlin, Germany

of nanometers.[8] In 4D-STEM a convergent electron beam with down to subnanometer (or even sub-Ångström) size is sequentially rastered over an electron-transparent sample area and the transmitted electrons are recorded in an angle-resolved manner at each scan position with an electron-sensitive camera. The electron beam is scattered at each sample position by the probed sample volume. This strong interaction encodes local sample properties in the transmitted electrons, which form a diffraction pattern (DP) on the camera. The so generated DP at each scan position results in a 4D-STEM dataset consisting of several thousand electron DPs depending on the scan grid size. A 4D-STEM dataset represents data along the two scan axes and two camera image axes, hence the "4D" in 4D-STEM. Analyzing these large datasets allows to map sample properties and local variations thereof over the whole scan area.[8] Different local properties can be extracted from each DP, for example crystal symmetry, crystal lattice parameters, crystal orientation, and strain, to name a few.[8] This access to properties that require the contribution of every atom in the structure, and not just the surface, is, in the context of the current work, a major advantage over scanning probe microscopies, such as scanning tunneling microscopy (STM) or atomic force microscopy (AFM).

The large amount of data generated by 4D-STEM can be challenging to handle since the raw data size can exceed the memory of many desktop computers. Furthermore, their rich information content can be challenging to extract and complex data analysis methods can be overwhelming to implement. Fortunately, there are several open-source Python packages, which are steadily developed further, that can process these datasets, including some which are capable of processing datasets that are larger than the computer's random-access memory (RAM). Open source Python packages include LiberTEM, py4STEM, pyxem, and many more.[9–11]

1.2. 4D-STEM with a Regular Scanning Electron Microscope

4D-STEM can also be implemented in regular scanning electron microscopes (SEMs) by mounting the sample such that electrons can pass through it and placing a camera below the electron-transparent sample.[12–16] Doing so expands the wide range of possible applications of SEMs further.

The lower beam energy of at most 30 keV of SEMs compared to the 30–300 keV of regular (scanning) transmission electron microscopes ((S)TEM) leads to an increased scattering cross section, amplifying the scattering signal and therefore the diffraction intensities.[17] Even 2D materials consisting of just a monolayer of light chemical elements, like graphene, can be mapped and imaged at these accelerating voltages.[18] A further benefit of lower electron beam energies is the reduced knock-on-damage. Graphene, for example, can be imaged without inducing defects at 80 keV and below.[19]

(S)TEMs can focus the electron beam to a smaller spot size than SEMs enabling atom-resolved imaging with up to sub-Ångström resolution. To achieve atom-resolved imaging, both, a higher electron beam energy and a higher electron beam convergence angle than what is typically available in an SEM, is needed.[20–22] A higher beam energy is also beneficial in

transmitting through thicker (3D) samples.[23] In the case of many beam-sensitive materials, it is not possible to directly image the atomic structure by STEM, since the high electron dose (number of electrons per area) required for imaging the structure at high resolution results in increased beam damage.[24–26] For crystalline materials, one may integrate images of many identical unit cells in order to improve the signal. Since for a given electron dose the counts in this integrated image increase linearly with the number of unit cells, the signal-to-noise-ratio (SNR) increases as the square root of the number of unit cells. In electron diffraction, the intensity for a given electron dose on the sample is proportional to the square of the number of unit cells being illuminated coherently; thus, the SNR increases linearly with the number of coherently illuminated unit cells. Electron diffraction is thus an attractive technique to obtain structural information from beam-sensitive samples, since a larger electron beam probe size compared to atom-resolved STEM imaging is capable of distributing the electron dose over several unit cells.[25–27]

Despite their lower accelerating voltage, SEMs may still have sub-nanometer spatial resolution, being fully sufficient for mapping sample properties on a nearly unit cell scale by 4D-STEM. Another advantage of SEMs is their larger scan area of several mm^2 compared to (S)TEMs (scan) image areas of several $100\,\mu m^2$. The larger scan size enables imaging of whole 3 mm-wide TEM grids without image stitching.

1.3. 4D-STEM-in-SEM to Characterize 2D Materials and 2D-like vdWH

The large scan area of SEMs can help in investigating the long-range order of 2D materials and 2D-like vdWH and their inherent thickness of only several nanometers makes them inherently electron-transparent, when free standing or when transferred onto the thin membrane of a TEM grid.

The lower beam energy and therefore stronger scattering, the large scan area size, and the potentially sub-nanometer spatial resolution make 4D-STEM-in-SEM an ideal tool to map properties of 2D materials and 2D-like vdWH.

2D materials were investigated with 4D-STEM-in-SEM with lens-coupled cameras and a MiniPIX hybrid-pixel detector from ADVACAM (Timepix 1-based direct detection camera with USB 2.0 connection that can count single electrons with a maximum of ≈45 frames per second (fps)).[12,15,16] Other existing camera-based diffraction techniques in SEMs are electron backscatter diffraction (EBSD) and transmission Kikuchi diffraction (TKD).[14,28–30] Powder nanobeam diffraction of particles on a TEM grid membrane with a SEM using a Timepix 1-based hybrid-pixel detector was also shown.[31] Single transmission electron DP acquisition was reported before in combination with STEM detectors.[32–35] To our knowledge 4D-STEM-in-SEM of 2D materials and 2D-like vdWH with a fiber-coupled camera was not reported so far.

We briefly present our unique system for 4D-STEM-in-SEM, show the single crystallinity of gold-exfoliated MoS_2 over a large area (more than $2\,mm^2$), and finally map the local structure of evaporated C60 molecules on MoS_2.[36]

2. Experimental Details

We applied our in-house developed system to acquire 4D-STEM datasets in a SEM.

The (substage) system is mounted on top of the sample stage of a SEM (GeminiSEM500, Carl Zeiss AG, Oberkochen, Germany) by sliding it onto the SEM stage dovetail mount. The transmission diffraction stage (TDS), a schematic of which is shown in **Figure 1**, comprises an electron-sensitive camera, a hexapod sample stage for moving the sample with 6 degrees of freedom, a detachable sample holder for TEM grids, a linear stage which holds the camera, an adapter for the Zeiss dovetail mount, and parts out of copper to dissipate heat from the camera to the SEM sample chamber, as well as control hardware outside of the chamber.

The electron-sensitive camera is a fiber-coupled scintillator-based camera developed in-house with a size of $25 \times 25 \times 11\,mm^3$. The hexapod stage holds the sample holder and fits between the SEM stage and the SEM pole piece without modifications to the SEM itself.

The camera is inside the hexapod stage and is attached to a linear stage. This linear stage allows for different distances between sample and camera, thus changing the camera length. More specifications of the TDS, including camera parameters and hexapod tilt range, are listed in the Experimental Section.

The control hardware outside of the SEM sample chamber comprises a control PC, an in-house developed scan generator, an electrostatic beam blanker, and controllers for the hexapod and the linear stage. The control PC is connected to the SEM PC, the camera, the stage controllers, and the scan generator. A C# library combines the control for all parts via their respective application programming interfaces (APIs), providing scripting access for starting a 4D-STEM scan for example.

The scan generator is connected to the camera's hardware trigger, to the SEM's external scan interface, to the detector outputs, and to the electrostatic beam blanker. The electrostatic beam blanker unblanks the electron beam at each scan position while the camera frame is active. A 4D-STEM scan employs these features to hardware synchronize the beam movement with the camera acquisition, the beam blanker, and the SEM detector acquisition.

The LiberTEM software running on the control PC is used to prescreen datasets and to store initial results.[9]

It is important to keep the TDS constantly under vacuum, also when not in use within the SEM, and to ideally plasma clean or to bake samples to 120 °C under vacuum before measurements to reduce carbon contamination from hydrocarbons.

3. Results

3.1. In-Plane Orientation of MoS₂ Obtained By Gold-Mediated Exfoliation

We investigated the in-plane orientation of MoS_2, which was exfoliated via gold-mediation as reported by Heyl et al.[36,37] **Figure 2**a shows an optical image of the investigated MoS_2 sample spanning $\approx 64\,mm^2$ on a Si wafer with a PMMA support
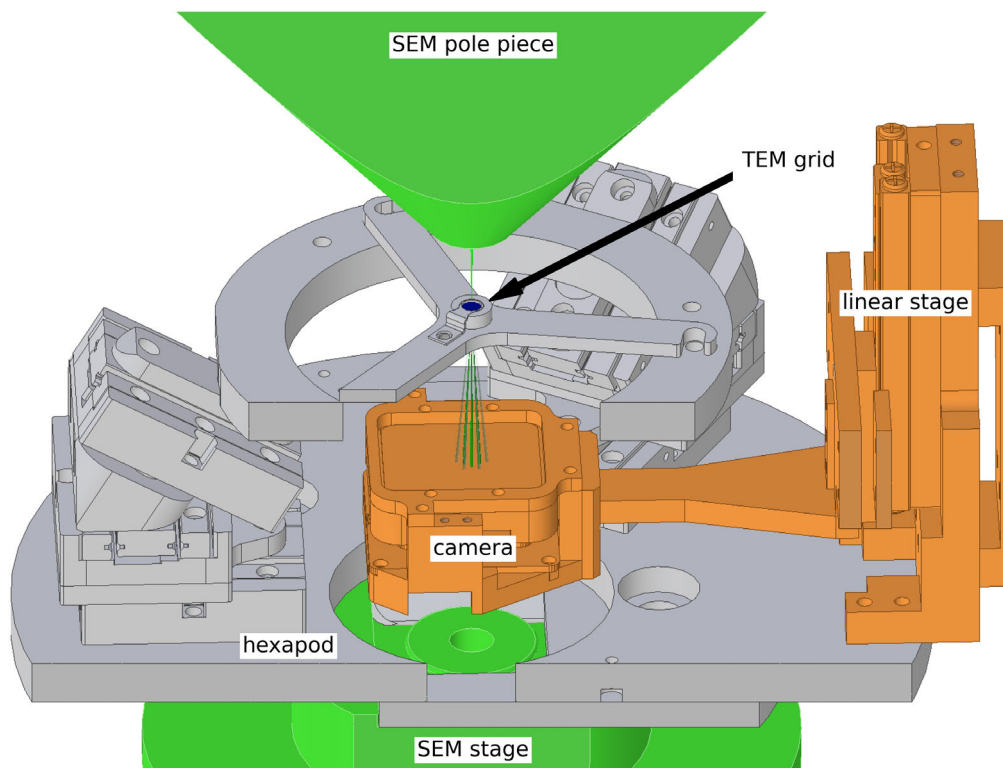

Figure 1. Schematic of the TDS. The electron beam is rastered sequentially over the sample area on the TEM grid and the corresponding DPs are recorded on the camera.
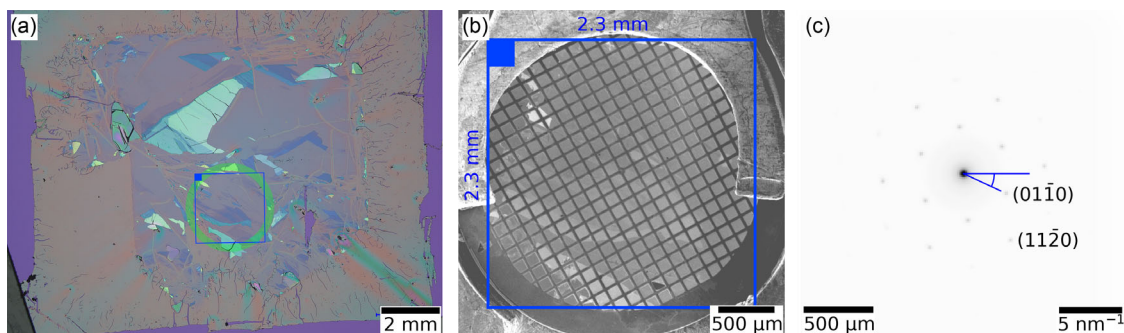
Figure 2. a) Optical image of MoS$_2$ exfoliated via gold-mediation between a PMMA film (on top) and a Si wafer (below). The area in the green circle was transferred to a Quantifoil TEM grid and the in-plane orientation of MoS$_2$ in the blue square was determined. b) SEM secondary electron (SE) image at 5 keV of the TEM grid with the transferred MoS$_2$ inside the TDS sample holder. The 4D-STEM dataset was acquired in the blue square. c) The average shift-compensated DP of the acquired 4D-STEM dataset on a log scale viewed along the [0001] zone axis of MoS$_2$ and the in-plane orientation angle convention, this angle convention is used for all other figures as well.

layer on top. The area indicated by a circle was transferred onto a Quantifoil TEM grid via the polymer-based transfer as described in the Experimental Section. Figure S1a, Supporting Information, shows an optical image of the TEM grid with transferred MoS$_2$.

A 4D-STEM dataset of the area in the blue square in Figure 2a, b was acquired using an electron beam energy of 20 keV, an electron beam current of 24.9 pA, a semiconvergence angle of 1.4 mrad, a camera length of 10.56 mm, and 1 ms camera exposure time per DP. A total of 192×192 scan points corresponding to 36 864 images of 800×800 camera pixels were recorded at 200 fps in 185 s (1 ms exposure, 4 ms blanked), resulting in 23 GBs of raw data. Covering an area of 2.3×2.3 mm^2, the average electron dose on the sample was about 1.1×10^{-5} electrons Å^{-2} or 1 electron per 924 nm^2. The camera frame rate was limited by the rate at which the camera can transfer data and the fact that, because of the movement of the DP on the camera induced by the large-area scan, we had to select a relatively large camera

area (800×800 pixel $= 4.7 \times 4.7$ mm^2). The sum of the acquired DPs is shown in Figure S1b, Supporting Information. Using the hexapod stage to translate the sample out of the field of view of the electron beam, a reference scan using 48×48 scan points has been acquired. This allowed for easy fitting and compensating of the beam movement on the camera by shifting the undiffracted beam to the image center. Figure 2c shows the shift-compensated and averaged DP, indicating also the in-plane orientation of the MoS$_2$ crystal. We extracted the diffraction peak positions in polar coordinates and corresponding peak intensities from the shift-compensated DPs.

Figure 3 shows the results of the analysis. The presented in-plane angle is the mean of the polar angles of all found diffraction peaks modulo 60° within a range of 3.47 and 3.84 nm^{-1} from the undiffracted beam, and the first diffraction order of MoS$_2$ lies in this range (in-plane lattice constant of MoS$_2$: 0.316 nm). The standard deviation (SD) of the in-plane angle is the SD of the polar angles of all found diffraction peaks modulo 60° in the same range.
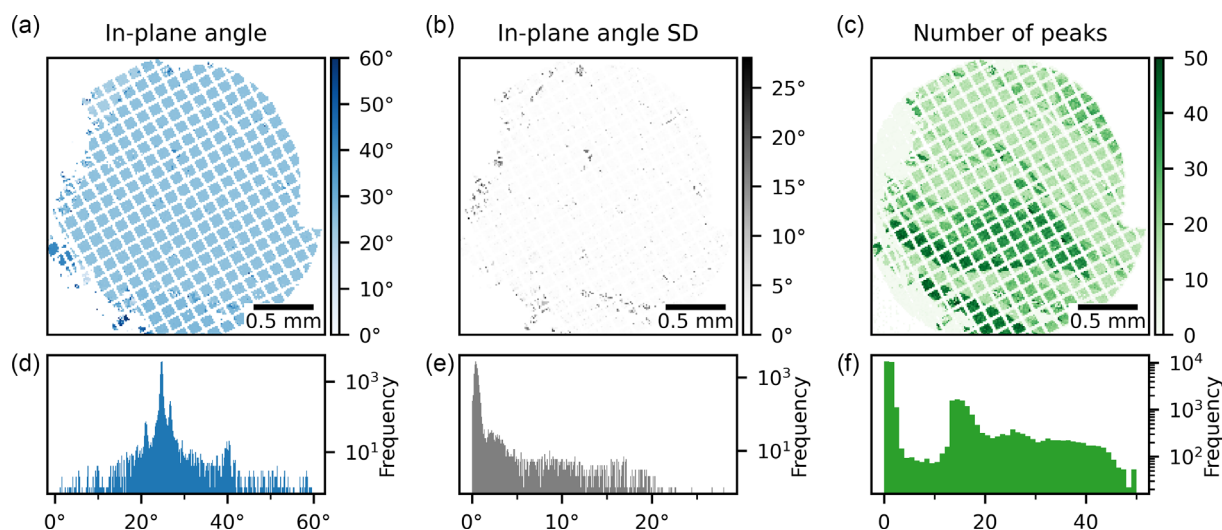

Figure 3. Results of the investigated TEM grid area shown in Figure 2. a) In-plane orientation of MoS$_2$ on the TEM grid, Figure 2c indicates the in-plane angle convention. b) SD of the in-plane orientation in a), c) number of found diffraction peaks, d–f) histogram of the in-plane angle, SD, and the number of found diffraction peaks respectively.

The exfoliated MoS$_2$ shows nearly a single in-plane rotation with a mean at 24.8° and a low SD (maximum at 0.4°) over the whole TEM grid, revealing its single crystallinity.

Figure S2, Supporting Information, shows simulated DPs of mono- to trilayer MoS$_2$ with 20 keV electron beam energy and 1.4 mrad semi-convergence angle (same as the experimental settings) confirming the increase in the diffraction peak intensity of higher-order diffraction peaks with the number of MoS$_2$ layers. The abTEM Python library was used for this simulation.[38] The number of MoS$_2$ layers contributing to each DP has not been retrieved, since the MoS$_2$ varies between being free standing or supported by the TEM grid membrane which also changes the peak intensity. The peak intensity ratio of the first- and second-order diffraction peaks in the simulation is around 1.8 for both mono- and bilayer MoS$_2$. The third-order diffraction peaks of monolayer MoS$_2$ are only barely, or not at all visible with the chosen experimental settings, making it prohibitively difficult to reliably quantify the number of layers.

The areas with multilayers possess the same in-plane angle and same SD, revealing that they exhibit the same orientation as the monolayers. Some corners of the transferred MoS$_2$ regions show a different in-plane orientation or a higher SD; this is likely caused by the polymer-assisted transfer onto the TEM grid; in these areas MoS$_2$ might fold onto itself or small cut-out areas of the MoS$_2$/polymer foil orient themselves differently when scooped from floating on water onto a TEM grid.

3.2. 5 nm of C60 Grown on MoS$_2$

We prepared a TEM grid with exfoliated MoS$_2$ from the same wafer shown in Figure 1a and evaporated an ≈5 nm thick layer of C60 molecules on the MoS$_2$; more details are given in the Experimental Section.

Our goal is to map the C60 coverage, grain structure, and the in-plane lattice orientation of C60 and multilayer MoS$_2$ to show possible applications for 4D-STEM-in-SEM on 2D-like vdWH.

Bulk C60 forms a cubic-close-packed (ccp) structure (face-centered-cubic (fcc) lattice ABC stacking) with a lattice constant $a = 1.426$ nm. The {111} planes are close packed and are $a/\sqrt{3} = 0.825$ nm apart.[39,40] Hybrid vdWHs of MoS$_2$ and C60 molecules were investigated before, for example, Sakurai et al. characterized the crystalline structure from C60 monolayers to 100 nm thick films on cleaved MoS$_2$ surfaces (MoS$_2$ (0001) plane) by reflection high-energy electron diffraction (RHEED).[41,42] The C60 molecules formed a close-packed structure with a nearest neighbor distance of 1.005 ± 0.015 nm, matching the bulk value of 1.002 nm and the close-packed (111) plane and [1$\bar{1}$0] zone axes of the C60 crystal lattice were parallel to the (0001) plane and [11$\bar{2}$0] zone axes of the MoS$_2$ crystal lattice respectively.[41,42] We can therefore expect with the bulk close-packed layer distance of 0.825 nm that the 5 nm thick C60 layer forms ≈6 close-packed (111) layers on the exfoliated MoS$_2$ surface ((0001) plane).

The investigated 4D-STEM dataset was acquired using an electron beam energy of 20 keV, an electron beam current of 29.3 pA, a semiconvergence angle of 2 mrad, a camera length of 20.56 mm, and 10 ms camera exposure time per DP. A total of 120 × 120 scan points corresponding to 14 400 images of 512 × 512 camera pixels were recorded at 80 fps in 180 s

(10 ms exposure, 2.5 ms blanked), resulting in 7.4 GBs of raw data. Covering an area of 1.4×1.4 μm^2, the average electron dose on the sample was about 140 electrons Å^{-2}. We chose a scan area of 113 × 113 scan points from the dataset.

Figure 4a shows a virtual dark field (vDF) image of the investigated area; each pixel is the sum of the intensity inside a ring with inner radius indicated with the dotted red arc and outer radius indicated by the dotted blue arc in Figure 4b of the corresponding DPs. The vDF image shows the MoS$_2$ multilayer suspended over a hole in the membrane of the Quantifoil TEM grid. The intensity differences around the edge of the hole originate from stronger scattering due to the thicker membrane at the edge than between holes.[43] Figure 4b shows the sum of the logarithm (logsum) of every DPs; we chose the logsum since it highlights weaker features better compared to the logarithm of the sum of DPs. The diffraction peaks of the crystalline phase of C60 molecules and of the MoS$_2$ layer are indexed; they form a hexagonal pattern as expected from previous reports.[41,42]

We computed the sixth-order radial Fourier analysis (RFA) between a ring indicated by the dotted red arc and solid red arc in Figure 4b with the LiberTEM Python package.[9] The strength of the sixth-order RFA is a measure for the presence of sixfold symmetry, an amorphous area results in a weaker and a crystalline area in a stronger value. The RFA indicates that the C60 molecules form dispersed crystalline areas with varying degrees of crystallinity on the suspended MoS$_2$ layer. The amorphous TEM grid membrane increases the diffuse background in the DPs, but has only a minimal effect on the visible sixfold symmetry.

The DPs in Figure 4f are from the area with the largest sixth-order RFA value (indicated by a red arrow in Figure 4c–f); Figure 4f is displayed in more detail in Figure S3, Supporting Information. The fainter peaks around the {11$\bar{2}$0} diffraction peaks of MoS$_2$ are Moiré peaks of the C60 lattice since the electrons scattering from the C60 layer may as well be scattered by the MoS$_2$ layer. In Figure 4f, the highlighted diffraction peaks are separated and confirm their cause. Remškar et al. also observed Moiré peaks although in a composite MoS$_2$-C60 crystal.[44]

We analyzed the in-plane orientation of C60 and MoS$_2$ further by applying the orientation mapping methods of the py4DSTEM Python package.[10] We selected a region of 160 × 160 camera pixels centered around the undiffracted beam, which includes the {2$\bar{2}$0} diffraction peaks of the C60 fcc lattice, to investigate the C60 in-plane orientation. We selected this smaller region to prevent potential orientation mismatches due to the presence of the MoS$_2$ lattice. Figure 4d shows the single orientation of the MoS$_2$ lattice, there are some variations at the edge of the hole in the support membrane of the TEM grid, likely caused by a combination of strain and electron beam broadening due to thickness differences of the TEM grid membrane. Figure 4e displays the in-plane orientation of the C60 lattice, the diffraction intensity was too faint or not present in the white areas. These areas coincide with a low sixth-order RFA value in Figure 4c, indicating a very faint crystalline C60 coverage or none at all.

The in-plane orientation of the C60 molecules varies stronger than the MoS$_2$ in-plane orientation, which could be caused by their lattice mismatch and surface contamination. The average
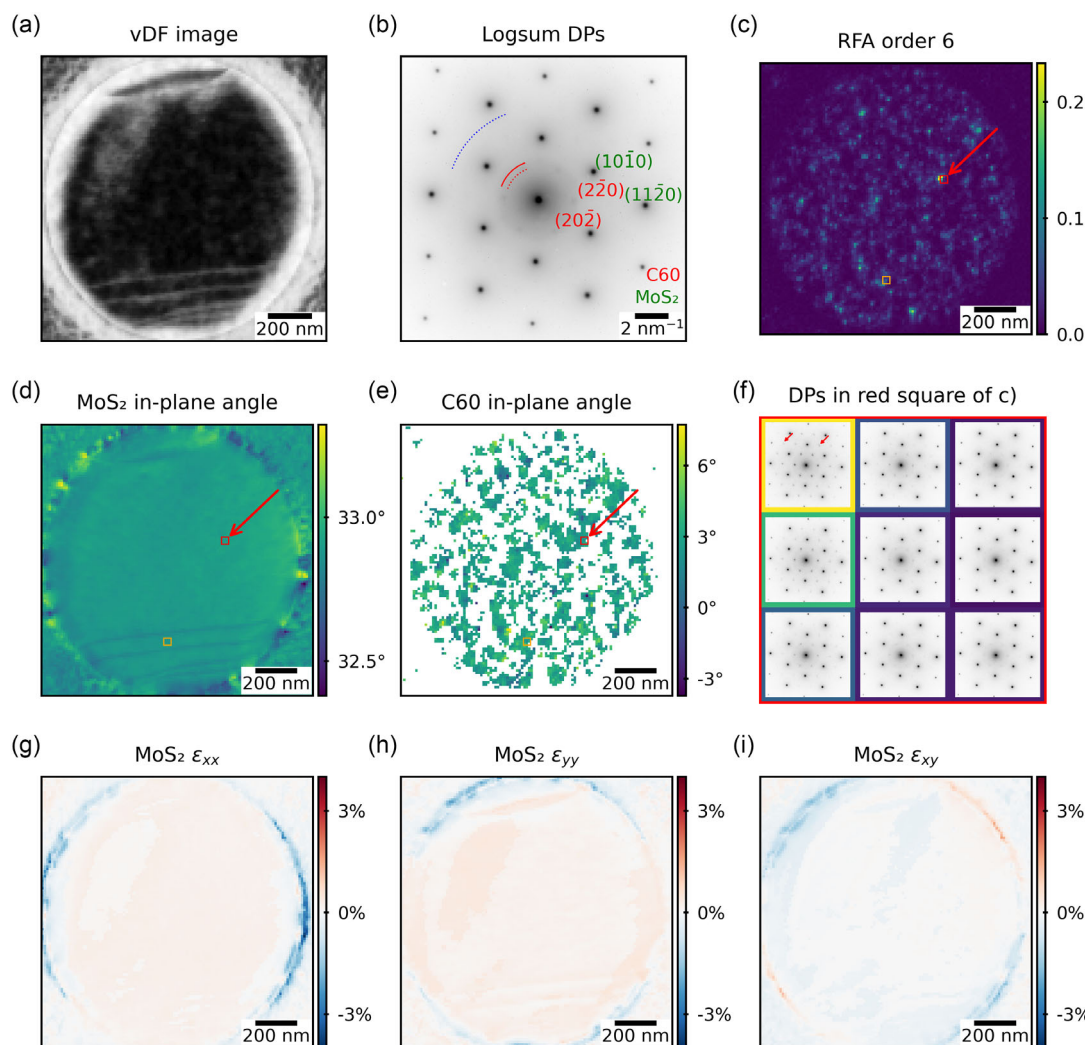
ADVANCED
SCIENCE NEWS
www.advancedsciencenews.com

physica
status
solidi a
www.pss-a.com

Figure 4. Results of the sample with C60 molecules on a MoS_2 multilayer. a) vDF image of the investigated area, showing the freestanding MoS_2 layer over a hole of the Quantifoil TEM grid membrane. The inner radius of the ring-shaped vDF detector is indicated by the dotted red arc and the outer radius is indicated by the dotted blue arc in (b). b) Logsum of all DPs with indexed diffraction peaks (C60 fcc in [111] zone axis and MoS_2 in [0001] zone axis). The C60 molecules form a hexagonal lattice in-plane which is aligned to the MoS_2 in-plane lattice: C60 fcc ($2\bar{2}0$) || MoS_2 ($11\bar{2}0$) (discussed in more detail in Figure 6. c) RFA of the sixth order between a ring indicated by the dotted red arc and solid red arc in (b) showing the C60 crystalline phase coverage; a DP in the lower orange square exhibited diffraction peaks indicating AB stacking. The orange square is displayed in Figure S4, Supporting Information. d,e) In-plane orientation of the MoS_2 and C60 lattice respectively. f) DPs of the area indicated with a red arrow and red square in (c) to (e), showing Moiré spots of the C60 lattice around the {110} MoS_2 diffraction peaks. The color of the frame around each DP corresponds to the RFA value in (c), the top left DP in (f) has the strongest RFA value in (c). Figure S3, Supporting Information, shows (f) in more detail. g–i) In-plane strain of the MoS_2 layer.

in-plane orientation of the MoS_2 lattice is $32.89 \pm 0.06°$ and of the C60 lattice is $(3 \pm 1°)$; the given errors are the respective SDs.

Figure 4g–i shows the measured in-plane strain of the MoS_2 layer; we analyzed the strain with the py4DSTEM Python package.[10] The strongest strain is at the edge of the hole in the supporting membrane on the TEM grid, since van der Waals forces pull the MoS_2 layer toward the walls of the hole.[45] The horizontal streaks in the ε_{yy} strain map are likely from a ruptured MoS_2 layer, surface contamination, or membrane buckling. The vDF image shows a stronger signal at these regions as well, but not between the streaks which excludes a difference in MoS_2 layer thickness. Strain measurements of

the C60 lattice are influenced by the close-by or overlapping Moiré peaks, affecting the retrieval of the overall peak location and resulting in an inaccurate strain measurement. Material compositions with nonoverlapping or weaker Moiré peaks, like C60 on a MoS_2 monolayer, should allow for an accurate strain measurement of both materials.

We analyzed the coverage and grain structure of crystalline C60 based on the connected areas in the C60 in-plane orientation analysis in Figure 4e. A C60 in-plane orientation was found in 34% of the suspended MoS_2 area and in 0.5% of the supported MoS_2 area; therefore, crystalline C60 is present in these areas although with a varying degree of crystallinity based on the

RFA analysis in Figure 4c. The surface roughness of the Quantifoil TEM grid membrane might cause the lower coverage in the supported MoS_2 area.[43] **Figure 5** shows an analysis of the grain structure of the grains with crystalline C60 (C60 grains). The average C60 grain size of all C60 grains is 2000 ± 6000 nm^2; the given error is the SD. We fitted C60 grains larger than four scan pixels (523 nm^2) with an ellipse, we excluded the smaller grains, since they would lead to discrete major axis angles of the corresponding ellipses. The average minor axis length is 60 ± 50 nm, the average major axis length is 110 ± 110 nm, the average aspect ratio is 1.9 ± 0.6, and the average major axis angle is $0 \pm 60°$; the given errors are again the corresponding SD.

Figure 6b shows a model of the proposed C60 fcc/MoS_2 structure derived from the experimental DP in Figure 6a. The epitaxial relation is C60 fcc ($2\bar{2}0$) || MoS_2 ($11\bar{2}0$) and C60 fcc [$1\bar{1}0$] || MoS_2 [$11\bar{2}0$], confirming earlier reports that both lattices are aligned.[41,42,44] The lack of the forbidden {$1\bar{1}0$} diffraction peaks of the C60 fcc lattice confirms that the C60 molecules assemble in the fcc bulk C60 lattice with its ABC stacking.[46] This observation fits with our earlier expectation that the 5 nm thick C60 layer consists of ≈6 close-packed layers (ABCABC sequence).

AB stacking corresponds to a hcp structure, where {$10\bar{1}0$} diffraction peaks (hcp lattice) should be visible.[46] The (0001) plane of a C60 hcp lattice and the (111) plane of a C60 fcc lattice are both close-packed.[46]

We also searched for areas were the C60 molecules might exhibit AB stacking by applying the RFA mentioned above, but with half the ring radius shown in Figure 4b to look for {$10\bar{1}0$} diffraction peaks of a C60 hcp lattice. The scan point with the largest RFA value in this ring is shown in Figure 6c, other areas show none or significantly lower intensity of these diffraction peaks. Figure 6d shows a model of the proposed C60 hcp/MoS_2 structure derived from the experimental DP in Figure 6c. The epitaxial relation is C60 hcp ($11\bar{2}0$) || MoS_2

($11\bar{2}0$) and C60 hcp [$11\bar{2}0$] || MoS_2 [$11\bar{2}0$]. In Figure 6c the C60 hcp {$11\bar{2}0$} diffraction peaks are stronger than the C60 hcp {$10\bar{1}0$} diffraction peaks which might indicate a mixture of C60 hcp and C60 fcc areas at this scan point, incomplete ABC stacking (e.g. an ABCAB sequence), or stacking faults (e.g. ABCABA).[46]

The DP in Figure 6c is located at the center of the orange square in Figure 4c–e. Figure S4, Supporting Information, shows the DPs corresponding to this square.

Figure S5, Supporting Information, shows simulated and indexed DPs of a ccp lattice (fcc–ABC stacking) and a hcp lattice (AB stacking) with unit cell parameters corresponding to the C60 nearest neighbor distance of 1.0 nm. We used the same acceleration voltage (20 kV) and C60 layer thickness (5 nm) as in the experimental settings for the simulation. In the hcp simulation, the {$11\bar{2}0$} diffraction peaks are stronger than the {$10\bar{1}0$} diffraction peaks, which might also explain the different intensities of these diffraction peaks in the experimental DP of Figure 6c.

4. Discussion and Conclusion

4.1. 4D-STEM-in-SEM in General

4D-STEM can map various structural properties of thin electron-transparent samples by recording several thousand transmission DPs. The atomic structure of several layers of the sample along the direction of the electron beam is encoded, since the electron beam probes the sample volume while passing through it. The sub-nanometer spatial resolution of SEMs and their large field of view spanning several millimeters allow to map sample properties on different length scales. 4D-STEM-in-SEM expands the vast application range of regular SEMs with an additional detector. It can offer analysis methods that are inaccessible in
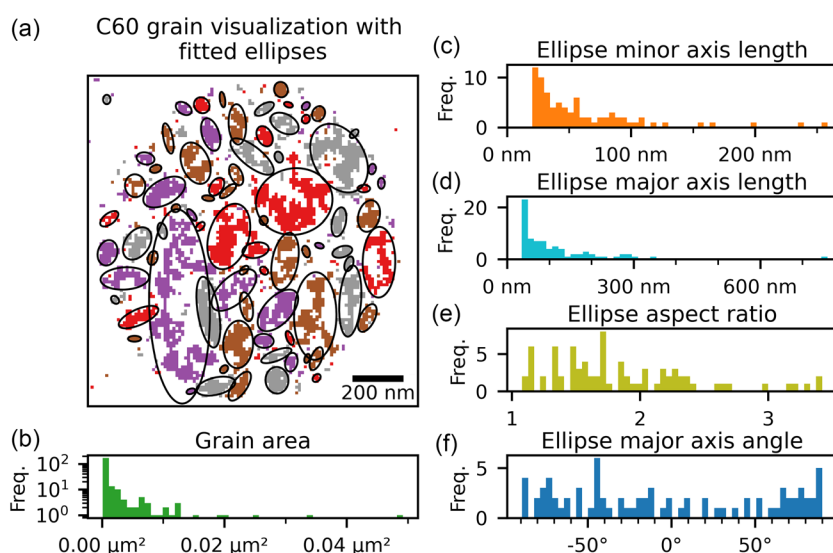

Figure 5. a) Visualization of the grains with crystalline C60 (C60 grains), neighboring grains are colored differently to visualize individual C60 grains better, and grains larger than four scan points (523 nm^2) are fit with an ellipse, the ellipses are drawn in black. b) Grain area distribution of all grains. c–f) Minor axis length, major axis length, aspect ratio, and major axis angle respectively of the fitted ellipses in (a).
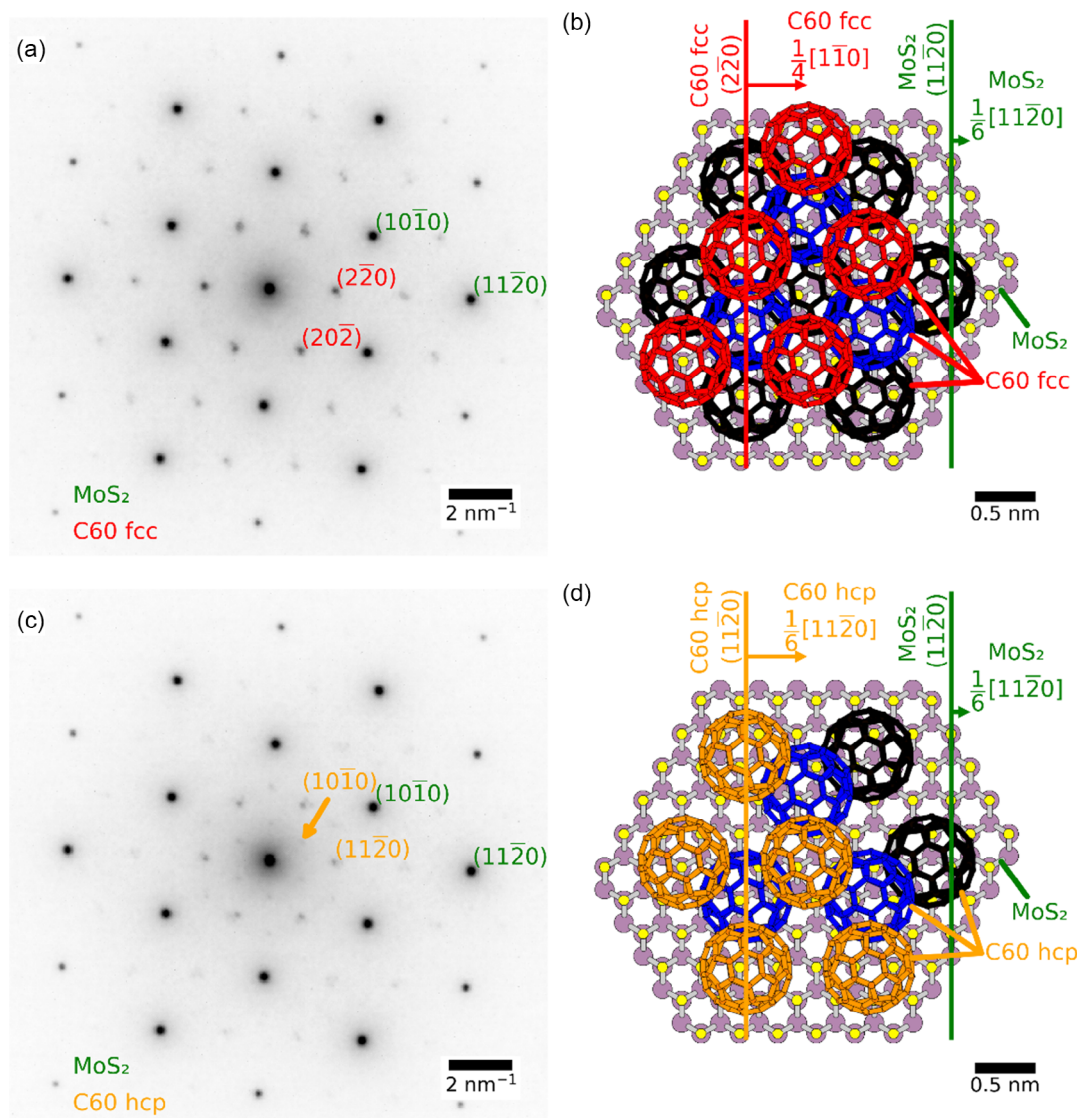
Figure 6. a) Indexed experimental DP with strongest RFA value in Figure 4c. This DP is located in the top-left scan pixel of the red square in Figure 4c–e. b) Model of the proposed C60 fcc (ABC stacking)/MoS$_2$ heterostructure showing the epitaxial relation derived from the DP in (a): C60 fcc ($2\bar{2}0$) || MoS$_2$ ($11\bar{2}0$) and C60 fcc [$1\bar{1}0$] || MoS$_2$ [$11\bar{2}0$]. c) Experimental DP with diffraction peaks corresponding to C60 hcp structure (AB stacking) {$10\bar{1}0$} diffraction peaks. This DP is located in the center scan pixel of the orange square in Figure 4c–e. The C60 hcp {$11\bar{2}0$} diffraction peaks are located at the same position as the C60 fcc {$2\bar{2}0$} diffraction peaks in (a). The C60 hcp {$11\bar{2}0$} diffraction peaks are stronger than the C60 hcp {$10\bar{1}0$} diffraction peaks; possible explanations are discussed in the main text. d) Model of a possible C60 hcp (AB stacking)/MoS$_2$ heterostructure which could explain the C60 hcp {$10\bar{1}0$} diffraction peaks in (c). The epitaxial relation is C60 hcp ($11\bar{2}0$) || MoS$_2$ ($11\bar{2}0$) and C60 hcp [$11\bar{2}0$] || MoS$_2$ [$11\bar{2}0$]. For (b) and (d): Not all C60 molecules are shown to improve the visibility of the stacking order, the vectors are orthogonal to the respective lattice plane and the length of the vectors indicates the distance between respective adjacent lattice planes.

standard SEM surface and morphology studies. 4D-STEM-in-SEM systems should be easily removable or retractable to guarantee regular SEM usability. They should allow for highest possible data acquisition rates and their integration should be seamless, like commercial EBSD systems.

Lens-coupled 4D-STEM-in-SEM systems might suffer from potential reflections of sidewalls or lens surfaces due to the strong nondiffracted beam. The potentially lower numerical aperture results typically in a lower detector efficiency compared

to fiber-coupled cameras or direct detectors. Furthermore, a compensation of lens aberrations might be required during or after data acquisition.

A SEM with a double-condenser system would be better for 4D-STEM-in-SEM, because the beam current can be changed separately from the convergence angle. An adjustable camera length in combination with a freely selectable convergence angle and beam current is beneficial. They allow changing the angular resolution in the DP, for example, to resolve diffraction from

large unit cells, and faster acquisition speeds by binning or by selecting a smaller region of interest, if the camera supports it.

4.2. 4D-STEM in SEMs Compared to STEMs

2D-like vdWH and other thin enough samples can be characterized by 4D-STEM in regular SEMs, especially if the required spatial resolution is in the nanometer range or above. Thicker samples and studies with atomic resolution require the higher beam energy and better spatial resolution of STEMs. Modifications on SEMs are simpler due the larger sample chamber and lower complexity of these instruments. (S)TEMs need a specific sample holder geometry and the space around the sample is limited to a few millimeters by the pole piece. Modifications are therefore more complex and might infringe on existing service contracts.

4.3. Electron Microscopy in General

Electron microscopy allows imaging with atomic resolution and spectroscopy with several meV energy resolution.[47] This results in a powerful, but often complex tool to characterize sample properties. For characterizing the atomic structure of a sample, electron diffraction is a well-suited method. While this technique is most sensitive to structural information within the plane that is normal to the direction of the electron beam, out-of-plane information is also encoded in the scattered electrons due to multiple scattering, but might be challenging to access. Multiple scattering can be enhanced by lowering the electron beam energy, and SEMs offer a freely selectable beam energy, whereas (S)TEMs have a discrete set of about 1–4 energies.

4D-STEM experiments with longer exposure times may suffer from carbon contamination during sample exposure, this is especially relevant in the lower vacuum of SEMs. The common methods to reduce carbon contamination like baking, cold traps, or plasma cleaning can be employed depending on the sample sensitivity. It is also possible to clean 2D materials inside the electron microscope using a micromanipulator.[48]

The requirement for electron-transparent samples is a detriment of TEM-samples need to be either free-standing or on top of an electron-transparent substrate. A broader range of samples is accessible to regular SEM studies and more surface-sensitive imaging methods like AFM. Several widely employed sample preparation methods do exist to render general samples accessible to TEM studies, but these methods are often destructive and/or hinder correlative measurements, for example, of devices. A possible method to transfer a sample from bulk substrates to a TEM grid and back includes etching a sacrificial copper layer.[49] Dedicated devices and other samples can also be manufactured directly on a TEM grid for correlative measurements, there are SiO_2 and SiN TEM grids with a RMS surface roughness of 0.65 nm.[50] Stacks of 2D materials and encapsulated samples can also be transferred.[51,52]

Low-electron energy microscopy (LEEM) and low-electron energy diffraction (LEED) probe the sample volume with a low penetration depth in reflection geometry, but it has a lower spatial resolution than TEM and is less common.[53–55] "4D"

scanning µ-LEED might be an exciting method to map sample properties similarly to 4D-STEM.

4.4. Outlook 4D-STEM-in-SEM

4D-STEM-in-SEM can also be applied in focused ion beam (FIB)–SEMs and is compatible with existing techniques for charge compensation, variable pressure, electrical contacting, nanomanipulators, and other in situ methods.

A rotation stage for tomography experiments at two or several angles might help in accessing out-of-plane information. For example, it might be possible to determine the out-of-plane nearest-neighbor spacing of the C60 molecules by tilting the sample toward the electron beam.

Single-electron-sensitive cameras like direct detectors or hybrid-pixel detectors with their faster acquisition speed should further expand the usability of 4D-STEM-in-SEM. However, some downsides of these cameras are their larger pixel size, which require a longer camera length if the angular resolution should be preserved, their larger physical size compared to scintillator-based cameras, and/or their limited electron counting rate, which make them less suitable for some applications. Direct electron detectors might also be insensitive to electrons with a beam energy of less than 15 keV due to their passivation layer. Scintillators are sensitive at lower voltages, but lose on the electron light conversion ratio.

5. Conclusion

4D-STEM is a powerful technique that is capable of retrieving a wide range of types of structural information about a given sample, also those that consist of multiple layers. 4D-STEM can also be employed in regular SEMs by placing an electron-sensitive camera below the sample. We deployed our own 4D-STEM-in-SEM system and showed the single crystallinity over several mm^2 of MoS_2 produced with gold-mediated exfoliation. We were also able to map properties of both layers of a C60/MoS_2 vdWH. 2D materials and 2D-like vdWHs are inherently electron-transparent due to their low thickness of just a few nanometers and are therefore ideal samples for 4D-STEM-in-SEM. The large scan area of SEMs and the nanometer-sized spatial resolution can help in investigating the long-range and medium-range order of 2D materials and 2D-like vdWH.

6. Experimental Section

TDS Specifications: Camera: Sony IMX174 CMOS sensor (1936×1216 pixels), 5.86 µm pixel size, P43 scintillator (1 ms decay time), ≈7 counts per 20 keV electron (calculated from image counts caused by a known electron current during 1 ms exposure, not by counting single electrons), (31 ± 1) counts per pixel in a dark reference image at 1 ms exposure time, bit depth: 12 bit (4096 counts), ≈295 fps at 512×512 pixels (12 bit per pixel), ≈70 °C sensor temperature when in vacuum, ≈50 °C when in ambient air. 5–36.5 mm camera length with hexapod at $z = 0$ mm.

TDS Specifications: Hexapod: SMARPOD 110.45 (SmarAct, Germany), minimal accessible movement range in z (beam direction): ±5 mm, in x and y: ±8.0 mm, minimal accessible sample tilt range about x and y at $x,y,z = 0$ mm (alpha and beta tilt): ±9.5°, sample rotation range about z at $x,y,z = 0$ mm: ±19.3°. The camera inside the hexapod limits the

movement and tilt range of the hexapod to the values listed above, since it can block the movement of the linear positioners of the hexapod.

TDS Specifications: Other: Maximum distance between sample and pole piece: $\approx$12.5 mm (hexapod at $z = 0$ mm and SEM stage at its lowest position).

Gold-Mediated Exfoliation of MoS_2: Polished silicon wafers were used as the ultraflat templates to deposit 200 nm Au via physical vapor deposition. As a mechanical support, glass chips were glued onto the gold-covered wafer with UV-cured epoxy resin. These gold–glass chips were cleaved off the wafer with a razor blade shortly before starting the exfoliation. The MoS_2 bulk crystal (2D semiconductors, synthetic MoS_2 crystal) was cleaved with heat-resistant Kapton tape to reveal a fresh crystal surface and then pressed onto the template-stripped gold substrate. The stack was annealed on a hotplate in ambient at 150 °C for 1 min. After a short cool down period of $\approx$15 s by removing the stack from the hotplate, the tape was peeled to finish the exfoliation. For further details we refer to earlier reports.[36,37]

Polymer-Based Transfer of MoS_2: Polystyrene (PS) and poly(methyl methacrylate) (PMMA) were used to transfer the exfoliated MoS_2 onto the TEM grids. The PS-based transfer was adapted from previous work.[56] PS was spin coated (Sigma-Aldrich, average $M_w \approx 280\,000$, 90 mg mL^{-1} in toluene, 3000 rpm 60 s) onto the exfoliated MoS_2 on gold followed by an annealing step at 80 °C for 10 min. The substrate was floated on gold etchant (KI/I$_2$, Sigma-Aldrich) with the PS side up until the PS foil floated freely ($\approx$12 h). The polymer foil was scooped off the etchant using a clean SiO$_2$/Si wafer piece and washed in deionized water several times to clean off etchant residues. For the transfer onto the TEM grids (Quantifoil R0.6/1 S180-1 or Quantifoil R 1.2/1.3 S143-1, Plano GmbH, Wetzlar, Germany), a piece of the polymer foil was scratched out, then floated on water, and finally scooped with the TEM grid. The TEM grids with the polymer foil were placed on a hotplate for 1 h to remove water between polymer foil and TEM grid to prevent the polymer foil from separating from the TEM grid in the following step. The hotplate temperature started at room temperature and reached 100 °C after 8 min. Polystyrene was dissolved using toluene to remove the polymer film. The TEM grid was placed in an acetone bath afterward to remove toluene residue; then the acetone was exchanged with isopropanol to remove acetone residue. For PMMA (Kayaku 950 PMMA A6, 4 k rpm for 60 s, then baked after spin coating at 110 °C for 1 min), the transfer was performed analogously to the PS-based layer, using acetone to remove the polymer film.

C60 Growth: C60 (Sigma-Aldrich, product number 572 500–5 g, purity 99.9%) was evaporated in vacuum from resistively heated quartz crucibles at a nominal rate of 1 nm min^{-1}, as determined by a quartz crystal microbalance. The molecules were evaporated at room temperature and a base pressure of 10^{-9} mbar. The TEM grids were mounted in a self-made sample holder to place them into the growth chamber.

Electron Microscopy: All electron microscopy images and 4D-STEM datasets were acquired with a GeminiSEM500 (Carl Zeiss AG, Oberkochen, Germany), which had a one-condenser system resulting in a change in converging angle when selecting a different beam aperture for a different electron beam current. The 4D-STEM dataset of the MoS_2 exfoliated via gold-mediation was acquired in "Low Mag" mode to be able to image the whole TEM grid at once. The other dataset was acquired in "Resolution" mode.

Optical Microscopy: All optical microscopy images were taken using a VHX-7100 (Keyence, Osaka, Japan).

Supporting Information

Supporting Information is available from the Wiley Online Library or from the author.

Conflict of Interest

The authors declare no conflict of interest.

Data Availability Statement

The code for analyzing the datasets and generating the figures is available at https://gitlab.com/JohMu/tds_hios_manuscript. Related datasets are linked in this repository as well.

[1] A. K. Geim, I. V. Grigorieva, *Nature* **2013**, *499*, 419.

[2] J. Sun, Y. Choi, Y. J. Choi, S. Kim, J. H. Park, S. Lee, J. H. Cho, *Adv. Mater.* **2019**, *31*, 1803831.

[3] S. Wang, C. Chen, Z. Yu, Y. He, X. Chen, Q. Wan, Y. Shi, D. W. Zhang, H. Zhou, X. Wang, P. Zhou, *Adv. Mater.* **2019**, *31*, 1806227.

[4] D. Jariwala, T. J. Marks, M. C. Hersam, *Nat. Mater.* **2017**, *16*, 170.

[5] O. L. Krivanek, M. F. Chisholm, V. Nicolosi, T. J. Pennycook, G. J. Corbin, N. Dellby, M. F. Murfitt, C. S. Own, Z. S. Szilagyi, M. P. Oxley, S. T. Pantelides, S. J. Pennycook, *Nature* **2010**, *464*, 571.

[6] Y. Liu, N. O. Weiss, X. Duan, H. C. Cheng, Y. Huang, X. Duan, *Nat. Rev. Mater.* **2016**, *1*, 16042.

[7] X. Xu, Z. Lou, S. Cheng, P. C. Y. Chow, N. Koch, H. M. Cheng, *Chem* **2021**, *7*, 2989.

[8] C. Ophus, *Microsc. Microanal.* **2019**, *25*, 563.

[9] A. Clausen, D. Weber, K. Ruzaeva, V. Migunov, A. Baburajan, A. Bahuleyan, J. Caron, R. Chandra, S. Halder, M. Nord, K. Müller-Caspary, R. Dunin-Borkowski, *J. Open Source Software* **2022**, *5*, 2006.

[10] B. H. Savitzky, S. E. Zeltmann, L. A. Hughes, H. G. Brown, S. Zhao, P. M. Pelz, T. C. Pekin, E. S. Barnard, J. Donohue, L. R. DaCosta, E. Kennedy, Y. Xie, M. T. Janish, M. M. Schneider, P. Herring, C. Gopal, A. Anapolsky, R. Dhall, K. C. Bustillo, P. Ercius, M. C. Scott, J. Ciston, A. M. Minor, C. Ophus, *Microsc. Microanal.* **2021**, *27*, 712.

[11] D. Johnstone, P. Crout, M. Nord, C. Francis, J. Laulainen, S. Høgås, E. Opheim, B. Martineau, T. Bergh, E. Prestat, N. Cautaerts, S. Smeets, H. W. Ånes, A. Ross, J. Broussard, S. Collins, T. Furnival, J. Daen, I. Hjorth, M. Danaie, A. Herzing, E. Jacobsen, T. Poon, D. Tiarnan, H. Shuoyuan, J. Morzy, A. Iqbal,

T. Ostasevicius, M. Von Lany, R. Tovey, pyxem/pyxem: pyxem 0.14.2, Zenodo, **2022**, https://zenodo.org/record/2649351 (accessed: February 2023).

[12] P. Schweizer, P. Denninger, C. Dolle, E. Spiecker, *Ultramicroscopy* **2020**, *213*, 112956.

[13] J. Müller, B. Haas, W. Van den Broek, S. Shabih, C. T. Koch, *Microsc. Microanal.* **2020**, *26*, 1906.

[14] J. J. Fundenberger, E. Bouzy, D. Goran, J. Guyon, H. Yuan, A. Morawiec, *Ultramicroscopy* **2016**, *161*, 17.

[15] B. W. Caplins, J. D. Holm, R. M. White, R. R. Keller, *Ultramicroscopy* **2020**, *219*, 113137.

[16] A. Orekhov, D. Jannis, N. Gauquelin, G. Guzzinati, A. N. Mehta, S. Psilodimitrakopoulos, L. Mouchliadis, P. K. Sahoo, I. Paradisanos, A. C. Ferrari, G. Kioseoglou, E. Stratakis, J. Verbeeck, Wide Field of View Crystal Orientation Mapping of Layered Materials, arXiv, **2020**, https://doi.org/10.48550/arxiv.2011.01875 (accessed: June 2023).

[17] M. J. Peet, R. Henderson, C. J. Russo, *Ultramicroscopy* **2019**, *203*, 125.

[18] J. C. Meyer, C. Kisielowski, R. Erni, M. D. Rossell, M. F. Crommie, A. Zettl, *Nano Lett.* **2008**, *8*, 3582.

[19] J. C. Meyer, F. Eder, S. Kurasch, V. Skalalova, J. Kotakoski, H. J. Park, S. Roth, A. Chuvilin, S. Eyhusen, G. Benner, A. V. Krasheninnikov, U. Kaiser, *Phys. Rev. Lett.* **2012**, *108*, 196102.

[20] U. Kaiser, J. Biskupek, J. C. Meyer, J. Leschner, L. Lechner, H. Rose, M. Stöger-Pollach, A. N. Khlobystov, P. Hartel, H. Müller, M. Haider, S. Eyhusen, G. Benner, *Ultramicroscopy* **2011**, *111*, 1239.

[21] N. Dellby, L. Krivanek, D. Nellist, E. Batson, R. Lupini, *J. Electron Microsc.* **2001**, *50*, 177.

[22] M. Linck, P. Hartel, S. Uhlemann, F. Kahl, H. Müller, J. Zach, M. Haider, M. Niestadt, M. Bischoff, J. Biskupek, Z. Lee, T. Lehnert, F. Börrnert, H. Rose, U. Kaiser, *Phys. Rev. Lett.* **2016**, *117*, 076101.

[23] C. Kisielowski, B. Freitag, M. Bischoff, H. van Lin, S. Lazar, G. Knippels, P. Tiemeijer, M. van der Stam, S. van Harrach, M. Stekelenburg, M. Haider, S. Uhlemann, H. Müller, P. Hartel, B. Kabius, D. Miller, I. Petrov, E. A. Olson, T. Donchev, E. A. Kenik, A. R. Lupini, J. Bentley, S. J. Pennycook, I. M. Anderson, A. M. Minor, A. K. Schmid, T. Duden, V. Radmilovic, Q. M. Ramasse, M. Watanabe, et al., *Microsc. Microanal.* **2008**, *14*, 469.

[24] K. Murata, M. Wolf, *Biochim. Biophys. Acta BBA Gen. Subj.* **2018**, *1862*, 324.

[25] B. L. Nannenga, T. Gonen, *Nat. Methods* **2019**, *16*, 369.

[26] M. Gallagher-Jones, C. Ophus, K. C. Bustillo, D. R. Boyer, O. Panova, C. Glynn, C. T. Zee, J. Ciston, K. C. Mancia, A. M. Minor, J. A. Rodriguez, *Commun. Biol.* **2019**, *2*, 1.

[27] L. F. Drummy, J. Yang, D. C. Martin, *Ultramicroscopy* **2004**, *99*, 247.

[28] R. R. Keller, R. H. Geiss, *J. Microsc.* **2012**, *245*, 245.

[29] E. Brodu, E. Bouzy, J. J. Fundenberger, J. Guyon, A. Guitton, Y. Zhang, *Mater. Charact.* **2017**, *130*, 92.

[30] S. Vespucci, A. Winkelmann, K. Mingard, D. Maneuski, V. O'Shea, C. Trager-Cowan, *J. Instrum.* **2017**, *12*, C02075.

[31] M. Slouf, R. Skoupy, E. Pavlova, V. Krzyzanek, *Nanomaterials* **2021**, *11*, 962.

[32] C. Sun, E. Müller, M. Meffert, D. Gerthsen, *Microsc. Microanal.* **2018**, *24*, 99.

[33] J. Holm, *Electron. Device Fail. Anal.* **2021**, *23*, 18.

[34] C. Sun, E. Müller, M. Meffert, D. Gerthsen, *Adv. Struct. Chem. Imaging* **2019**, *5*, 1.

[35] B. W. Caplins, J. D. Holm, R. R. Keller, *Ultramicroscopy* **2019**, *196*, 40.

[36] M. Heyl, D. Burmeister, T. Schultz, S. Pallasch, G. Ligorio, N. Koch, E. J. W. List-Kratochvil, *Phys. Status Solidi RRL* **2020**, *14*, 2000408.

[37] M. Heyl, E. J. W. List-Kratochvil, *Appl. Phys. A* **2023**, *129*, 16.

[38] J. Madsen, T. Susi, *Open Res. Eur.* **2021**, *1*, 24.

[39] A. Kelly, K. M. Knowles, in *Crystallography and Crystal Defects*, Wiley, Hoboken, NJ **2012**.

[40] D. L. Dorset, M. P. McCourt, *Acta Crystallogr. A* **1994**, *50*, 344.

[41] M. Sakurai, H. Tada, K. S. Koichiro Saiki, A. K. Atsushi Koma, *Jpn. J. Appl. Phys.* **1991**, *30*, L1892.

[42] M. Sakurai, H. Tada, K. Saiki, A. Koma, H. Funasaka, Y. Kishimoto, *Chem. Phys. Lett.* **1993**, *208*, 425.

[43] R. Kazan, G. Bourgeois, D. Carisetti, I. Florea, E. Larquet, J. L. Maurice, Y. Mechulam, F. Ozanam, E. Schmitt, P. D. Coureux, *Front. Mol. Biosci.* **2022**, *9*, https://doi.org/10.3389/fmolb.2022.910218.

[44] M. Remškar, A. Mrzel, A. Jesih, J. Kovač, H. Cohen, R. Sanjinés, F. Lévy, *Adv. Mater.* **2005**, *17*, 911.

[45] C. Lee, X. Wei, J. W. Kysar, J. Hone, *Science* **2008**, *321*, 385.

[46] H. Kohl, L. Reimer, in *Transmission Electron Microscopy: Physics Of Image Formation*, Springer, New York, NY **2008**.

[47] O. L. Krivanek, *Microsc. Microanal.* **2021**, *27*, 3474.

[48] P. Schweizer, C. Dolle, D. Dasler, G. Abellán, F. Hauke, A. Hirsch, E. Spiecker, *Nat. Commun.* **2020**, *11*, 1743.

[49] M. Quincke, T. Lehnert, I. Keren, N. Moses Badlyan, F. Port, M. Goncalves, M. J. Mohn, J. Maultzsch, H. Steinberg, U. Kaiser, *ACS Appl. Nano Mater.* **2022**, *5*, 11429.

[50] Silicon Dioxide Support Films for TEM, https://www.tedpella.com/grids_html/silicon-dioxide.aspx (Accessed: February 2023).

[51] F. Pizzocchero, L. Gammelgaard, B. S. Jessen, J. M. Caridad, L. Wang, J. Hone, P. Bøggild, T. J. Booth, *Nat. Commun.* **2016**, *7*, 11894.

[52] A. J. Watson, W. Lu, M. H. D. Guimarães, M. Stöhr, *2D Mater.* **2023**, *8*, 032001.

[53] Z. Dai, W. Jin, M. Grady, J. T. Sadowski, J. I. Dadap, R. M. Osgood, K. Pohl, *Surf. Sci.* **2017**, *660*, 16.

[54] P. Schädlich, F. Speck, C. Bouhafs, N. Mishra, S. Forti, C. Coletti, T. Seyller, *Adv. Mater. Interfaces* **2021**, *8*, 2002025.

[55] F. Speck, M. Ostler, S. Besendörfer, J. Krone, M. Wanke, T. Seyller, *Ann. Phys.* **2017**, *529*, 1700046.

[56] M. Heyl, S. Grützmacher, S. Rühl, G. Ligorio, N. Koch, E. J. W. List-Kratochvil, *Adv. Mater. Interfaces* **2022**, *9*, 2200362.